



Segmenting nailfold capillaries using an improved U-net network

Shupeng Liu^{a,*}, Yuemei Li^a, Jingjing Zhou^b, Junwei Hu^a, Na Chen^a, Yana Shang^a, Zhenyi Chen^a, Taihao Li^{c,*}

^a Key Laboratory of Specialty Fiber Optics and Optical Access Networks, Joint International Research Laboratory of Specialty Fiber Optics and Advanced Communication, Shanghai Institute for Advanced Communication and Data Science, Institute of Biomedical Engineering, School of Communication and Information Engineering, Shanghai University, 333 Nanchen Road, Shanghai 200444, China

^b School of Life Sciences, Shanghai University, 333 Nanchen Road, Shanghai 200444, China

^c Zhejiang Lab, Institute of Artificial Intelligence, Hangzhou 401318, China

ARTICLE INFO

Keywords:

Nailfold capillaroscopy

Segmentation

U-Net

Res-Unet

ABSTRACT

To assess the microcirculation in a patient's capillaries, clinicians often use the valuable and non-invasive diagnostic tool of nailfold capillaroscopy (NC). In particular, evaluating the images that result from NC is particularly important for diagnosing diseases in which the capillary morphology is altered. However, NC images are generally of poor quality, such that analyzing them is difficult and time consuming. Thus, the purpose of this work was to determine a way to segment the capillaries in poor-quality NC images accurately. To do this, we proposed using a deep neural network with a Res-Unet structure. The network combines the residual network (ResNet) and the U-Net to establish an encoding-decoding network and to deepen the layers in the network to preserve the features of the deep layer. The network was trained on 30 nailfold capillary images to discriminate the pixels belonging to capillaries, and it was then tested on a dataset consisting of 20 images to achieve a binarized map. The mean accuracy was 91.72% and the mean Dice score was 97.66% compared to the ground truth, which indicates that using Res-Unet to perform capillary segmentation in NC images had good performance.

1. Introduction

Microcirculation, which refers to the blood circulation in arterioles, capillaries, and venules (Koscielny et al., 1998), allows human tissue cells to absorb nutrients, take up oxygen, and excrete metabolites (Tian and Li, 1992). To observe the microcirculation of capillaries and their morphology, clinicians use capillaroscopy, a simple and non-invasive tool that can be used to diagnose and identify autoimmune diseases that alter the microcirculation, e.g., Raynaud's phenomenon (RP), systemic sclerosis (SSc) and other rheumatologic diseases (Karbalaie, 2018; Mannarino et al., 1994; Cutolo and Smith, 2013). This technique is often applied to capillaries in the nailfold area, as they can be observed easily; hence, nailfold capillaroscopy (NC) is a valuable tool (Nivedha et al., 2016).

In the nailfold area, the classical physiological pattern of the capillary loop is a hairpin structure. A key criterion for distinguishing normal capillary morphology from abnormal capillary morphology is the convexity of the capillary head (Smith et al., 2016; Cutolo et al., 2018; Karbalaie et al., 2019). Other morphological features include the shape, distribution, and diameter of the capillaries as well as the density

of the capillary loops (Karbalaie et al., 2019; Faggioli et al., 2015). In conditions such as hypertension, diabetes, and heart disease, capillaries can become dilated and tortuous, and capillary microhemorrhages can occur (Bonacci et al., 1996). For example, patients with Raynaud's phenomenon frequently show an abnormal capillary pattern, including an altered arrangement of capillary loops, a decrease in the number of capillaries, and abnormal ramifications. Based on these features, clinicians have used NC to distinguish the primary Raynaud's phenomenon (RP) from the secondary RP in rheumatic diseases (Mannarino et al., 1994).

Although NC has shown promise for diagnosis, the associated poor-quality images – resulting from low-cost cameras, low-contrast images, image noise, dust on the lenses, the movement of patients' fingers during imaging, and air bubbles in the immersion oil – greatly hinder clinicians' abilities to differentiate between related diseases and to segment and measure the capillaries (Nivedha et al., 2016; Shigeharu et al., 2016; Li et al., 2017). To minimize the effect of poor-quality images, this work introduces a way to accurately segment capillaries on poor-quality NC images.

In previous literature, some approaches have been proposed to

* Corresponding authors.

E-mail addresses: liusp@shu.edu.cn (S. Liu), lith@zhejianglab.com (T. Li).

<https://doi.org/10.1016/j.mvr.2020.104011>

Received 16 October 2019; Received in revised form 28 April 2020; Accepted 28 April 2020

Available online 01 May 2020

0026-2862/ © 2020 Elsevier Inc. All rights reserved.

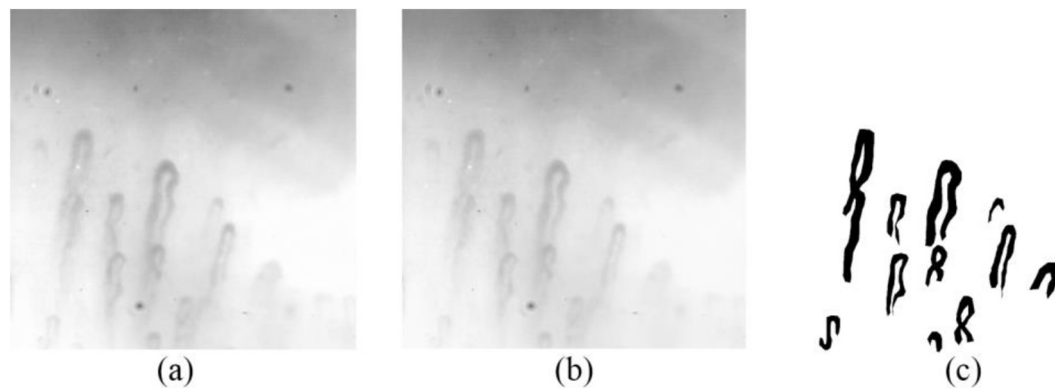


Fig. 1. Pre-processing the input image. (a) gray-scale input image. (b) green channel input image. (c) labelled image. (For interpretation of the references to colour in this figure legend, the reader is referred to the web version of this article.)

extract capillaries automatically. For example, as a pre-processing step for skeletonization of nailfold capillary images, N. P. Doshi et al. used an enhancement operation: They achieved the best performance with a simple α -trimmed filter to address non-uniform lighting combined with an iterative rule-based skeletonization procedure (Doshi et al., 2015). In another study, Arya Tama et al. processed nailfold capillaroscopy images using four steps: pre-processing, binarization, skeleton extraction, and skeleton segmentation, where morphological characteristics could be measured after binarization, skeleton extraction, and skeleton segmentation (Tama et al., 2015).

While the approaches in both of the above studies resulted in successful segmentation of the capillary profiles or extraction of the capillary skeletons, the NC images used in those studies had little background noise and were not poor quality. In practice, however, it is essential to segment capillaries in poor-quality NC images. One approach for analyzing poor-quality NC images might be to take advantage of developments in artificial intelligence. In particular, deep learning has already shown good performance in medical image processing (Shen et al., 2017; Lawrence Carin et al., 2018), especially regarding CNN (convolutional neural networks) (Haixiang et al., 2015; Soomro et al., 2017) and networks that have been improved further, such as FCN (fully convolutional network) (Shelhamer et al., 2017) and U-Net. These two improved networks offer pixel-level classification and can produce a prediction for each pixel while retaining the spatial information of the original input image. Thus, these networks might be able to significantly reduce the problems associated with image quality to ensure the consistency and reproducibility of capillary segmentation results.

This paper proposes a method of capillary segmentation based on Res-UNet to extract capillaries from background. The U-shaped structure is adopted from the FCN network, and it allows one to achieve more feature maps from deeper layers. The paper is summarized as three parts: Section one deals with the process of image acquisition and pre-processing; section two explains the segmentation algorithms used in the paper; and section three draws the conclusion, based on qualitative and quantitative comparison tests, that Res-UNet has good performance in the segmentation of nailfold capillary images.

2. Materials

2.1. Nailfold capillary data collection

There are no limits on the number of fingers or the number of fields that can be selected for examination; here, we examined the fourth finger (Karbalaie, 2018). Before the examination, patients were seated at room temperature (25–30 °C) for 15–20 min to be acclimatized and to relax (Etehad Tavakol et al., 2015). Then, the patient's hand (the one with less injury) was placed at heart level (Etehad Tavakol et al., 2015).

Some cedar oil was dripped on the surface of the skin at the root of the nail to increase transparency and reduce diffuse reflection. For imaging, we used a non-contact microcirculation microscope of type XW880 with an attached 5 million-pixel CMOS camera and white LED light source. The device worked at 380 \times magnification. The fourth finger was placed on the fixator of the device, and the focusing knob was adjusted. The CCD camera, installed and connected to the computer, was used to capture the best view of the capillary image per finger.

Sixty people aged 20–50 years old participated in the study, including 52 healthy subjects, 3 subjects with hypertension and 5 subjects with hypotension. 30 cases were used as the training set and 20 were used as the test set. The remaining cases were not used due to physically injured fingers and skin pigmentation. The training set was divided into images and labels that were marked by a professional.

2.2. Pre-processing

To construct the training and testing set for the U-Net network, the collected images data needed to be pre-processed. First, we manually cropped the region of interest on each image, and each cropped image had a uniform resolution of 512 \times 512. The acquired RGB capillary images had low contrast, but, as described in the literature, images in the green channel should show high contrast between capillaries and the background (Al-Gindya et al., 2008). Thus, we acquired green channel and gray-scale capillary images to compare for higher contrast. We found no significant difference in the contrast between the two images, and we eventually found that the gray-scale images were associated with better performance; nonetheless, green channel images may be more informative (Nivedha et al., 2016). Here, we used gray-scale images as input images.

The labels were made by Photoshop software, and the capillaries were marked. The white area represents the background and the black area represents the target area. The labelled image is shown in Fig. 1(c).

2.3. Data augmentation

The training dataset included 30 images. Some of the resulting label images were enhanced by horizontal flipping, translation, amplification, rotation and shear using the ImageDataGenerator function in Keras, as shown in Fig. 2, which makes the network more invariant and robust; vertical flipping was not performed, as this will change semantic information of the image in the object hierarchies (Li, 2011). During augmentation, in order to have the labelled image and the training image change synchronously, the training image's pixel value matrix was placed in the first channel, and the corresponding pixel value matrix of the labelled image was placed in the third channel, after which the channels were merged into a single image for data augmentation. After that, the training image and the labelled image were

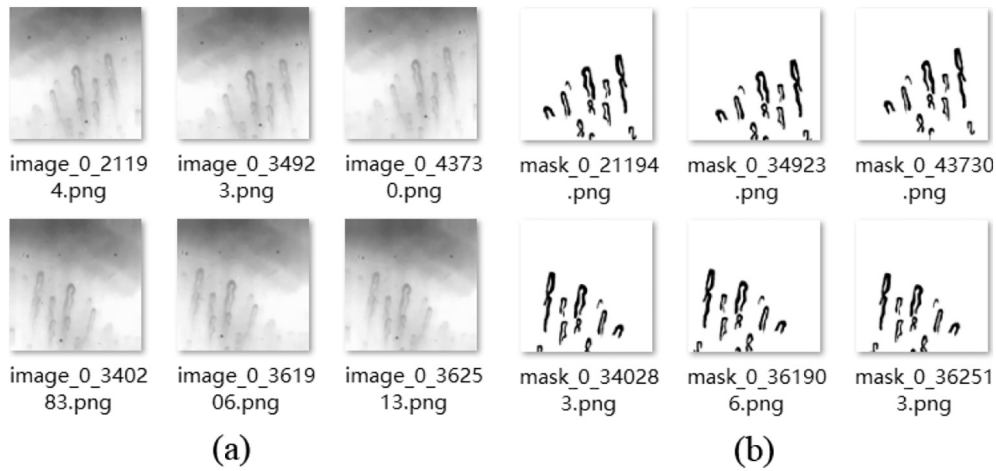


Fig. 2. Data augmentation images. (a) the gray-scale images. (b) the labelled images.

separated according to the channels. After augmentation, the number of images in the training set was 20664.

3. Methods

3.1. U-Net

The main features of U-Net are a U-shaped structure and long-connected leaping structure. U-Net is an encoder-decoder network that is shaped like the letter U, and it can be divided into a contraction path and an expansion path (Ronneberger et al., 2015). The contraction path is an architecture of the convolutions network, containing two repeated 3×3 convolutions and ReLU activation functions, followed by a 2×2 max pooling; the number of feature channels are doubled after each max pooling. The expansion path is symmetric to the contraction path. Each layer consists of a 2×2 up sampling, two 3×3 convolutions and ReLU activation functions (Ronneberger et al., 2015). The long-connected leaping structure can concatenate high-level semantics and information at low levels. A 1×1 convolution is used to map each 64-component feature vector to the corresponding classes at the end of the network (Ronneberger et al., 2015). U-Net can convolute images of any shape and size, which is especially useful for large medical images.

3.2. ResNet

The depth of the network has a great influence on feature extraction and classification (Zhang et al., 2019; Szegedy et al., 2015; Simonyan and Zisserman, 2014), as a shallow network has limited recognition capabilities. Capillaries with low contrast need deeper layers to extract more features. In theory, the deeper the network is, the better the network performs. But, in practice, the deepening of a network comes along with decreases in the accuracy of the training set, since the gradient disappears and the network has a worse response to the training (Bengio et al., 1994; Glorot and Bengio, 2010). This problem can be solved by using a residual network (ResNet) (Szegedy et al., 2016).

Regarding the problem of the training accuracy decreasing as the network deepens, ResNet provides two solution paths: identity mapping and residual mapping. When the network has reached its optimum balance between accuracy and deepening, the weights of the multiple nonlinear layers of residual mapping will be driven toward zero, leaving only identity mapping. So, once the network reaches its theoretically optimal state, the performance of the network will not decrease with an increase of depth (He et al., 2016a).

A new residual unit structure with better performance (He et al., 2016a; He et al., 2016b) is proposed based on the original unit structure, as shown in Fig. 3(b). The output is $H(x) = x + F(x)$ when the

number of layers is 1. The output of the last layer L (assuming that it starts at layer 1) is as follows:

$$H(x_L) = x + \sum_{i=1}^L F(x_i) \quad (1)$$

The characteristic $H(x_L)$ can be expressed as the sum of x and the residual function $F(x)$ between each layer, as shown in Fig. 3(c). It can be seen from the reverse derivation of the formula that the gradient will not disappear.

3.3. Res-Net

In view of the advantages of U-Net and ResNet, we propose a new deep neural network Res-Net (Ronneberger et al., 2015; He et al., 2016a). ResNet is used as the front-end feature extraction module, which is equivalent to down sampling (take ResNet18 as an example), to extract higher-level features (He et al., 2016b). The Res-Net neural network is shown in Fig. 4.

The Res-Net is composed of a coding part, a decoding part, and a long connection part. The coding part is where feature extraction occurs, in which high-pixel features are extracted from context by down sampling. Then, the decoding part returns to the classification of pixels. The long connection part functions to fuse the features extracted from the coding and the decoding parts to preserve as many details as possible.

In the coding part, two residual blocks are added to each layer. Each residual block contains two 3×3 convolution blocks and identity mapping. Different numbers of residual blocks compose different ResNets, such as ResNet18, ResNet34 and so on (Szegedy et al., 2015).

The decoding part also contains four layers, and each of these contains two residual units, forming a U-shaped structure where the decoding and coding parts are symmetric. Each layer is fused with a feature map from the corresponding layer of the contraction path. The leaping structure ensures the details. In order to ensure the same resolution in fusion, there is an up-sampling of the underlying feature map before each layer. The last layer is a 1×1 convolution and sigmoid activation layer for mapping multi-channel feature vectors to the required segmentation.

In the residual unit, batch normalization is equivalent to normalization, which means that the input of each layer of the neural network maintains the same distribution during the training of the deep neural network (Ioffe and Szegedy, 2015). The excitation function ReLU can also ensure that each layer of the network is still sensitive to input, and this helps the network maintain its gradient (Khan et al., 2019).

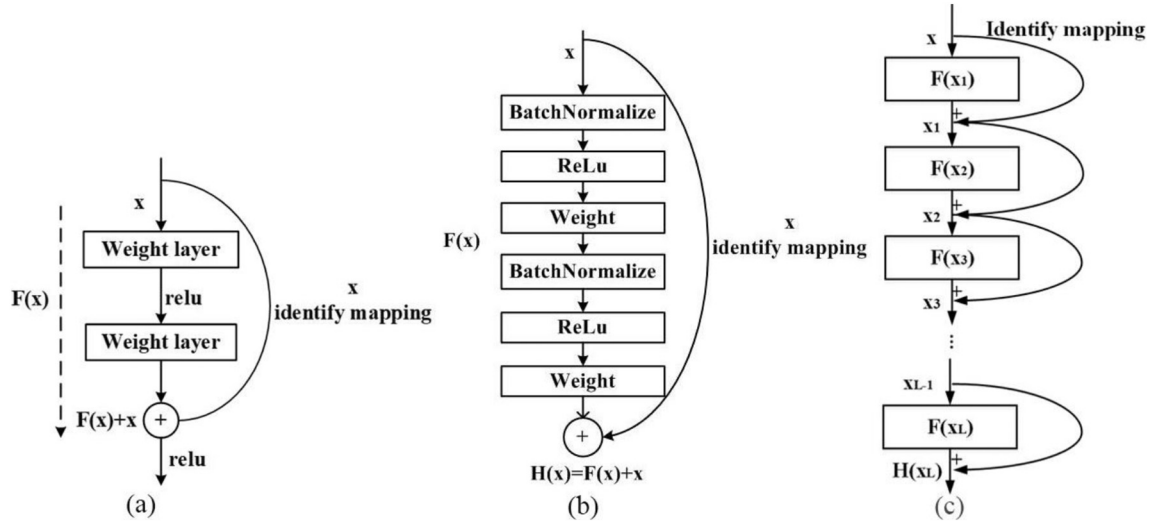


Fig. 3. Residual block. (a) original residual block (He et al., 2016a). The dashed line is the residual mapping. (b) proposed residual block. The curve is identity mapping, indicating the easiest paths for the information to propagate (He et al., 2016b). (c) the multi-layer network with residual blocks.

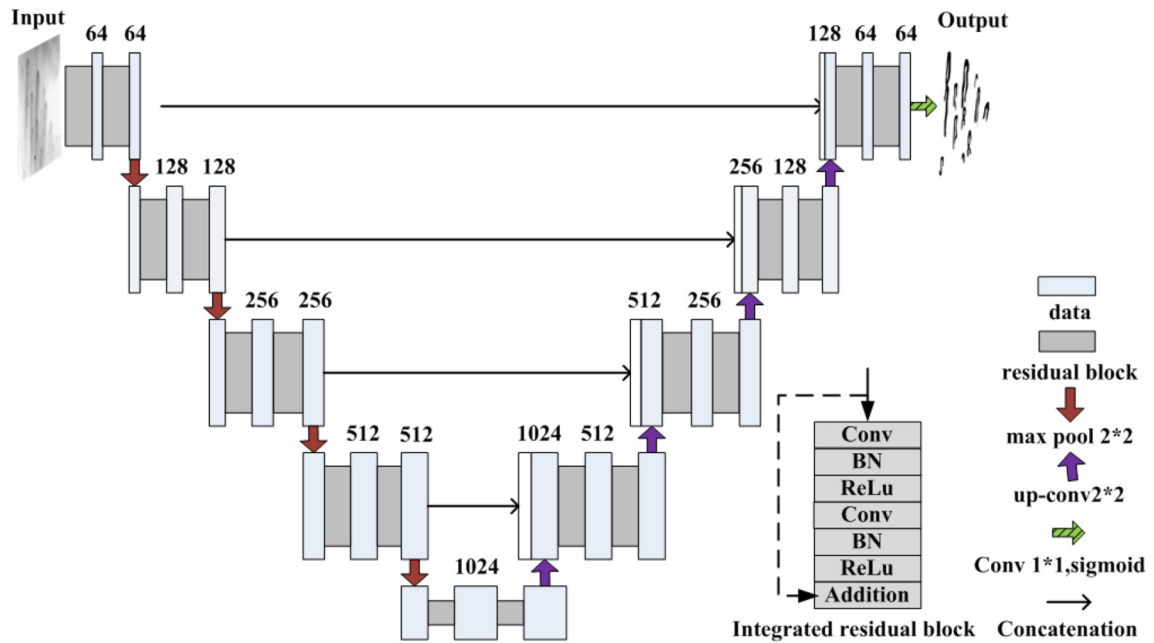


Fig. 4. The structure of Res-UNet18. A gray-scale image is the input and a binary image is the output. The light blue boxes correspond to multi-channel feature maps. The white boxes represent the concatenated copied feature maps from the contractive path. Two convolution layers, two BN layers, two ReLu layers, and an additional layer constitute an integrated residual block, represented by the gray areas. The residual block replaces the operations of convolution and ReLu activation function in U-Net.

Table 1
Accuracy of segmentation results.

	Median	Mean	SD
U-Net	86.90	86.24	1.74
Res-UNet18	91.32	91.72	1.39
Green channel	90.79	90.81	1.26
Res-UNet34	91.41	91.41	1.57

Green channel: For this model, input images of Res-UNet18 were in the green channel; the input images of other models were in gray scale. Accuracy (%): $(TP + TN)/(TP + TN + FP + FN)$; TP: true positive, actually positive, predicted positive; TN: true negative, actually negative, predicted negative; FP: false positive, actually negative, predicted positive; FN: false negative, actually positive, predicted negative; SD: standard deviation.

Table 2
Dice scores of segmentation results.

	Median	Mean	SD
U-Net	97.40	97.29	5.92
Res-UNet18	97.59	97.66	5.42
Green channel	97.28	97.34	5.83
Res-UNet34	97.23	97.39	6.14

Dice (%): $2TP/(2TP + FN + FP)$.

4. Results and analysis

To achieve a balance between network accuracy and training complexity, we have conducted many comparative experiments. Here we describe our results on the best network structure.

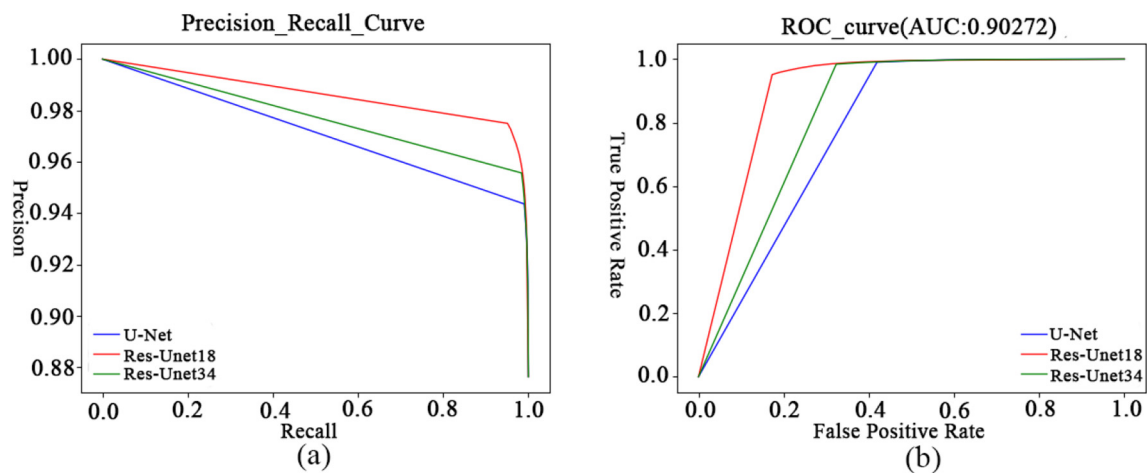


Fig. 5. Comparison of precision recall curves and ROC curves for the models. (a) Precision recall curves. Res-Unet18 has the highest precision rate or highest recall rate. (b) ROC curves. True Positive Rate (TPR): the rate of correctly predicted positive classes in all positive classes; False Positive Rate (FPR): the rate of predicted positive in all negative classes. The AUC value of the Res-Unet18 model is 0.9027 and convex to the upper left, meaning that the segmentation accuracy of Res-Unet18 was the highest.

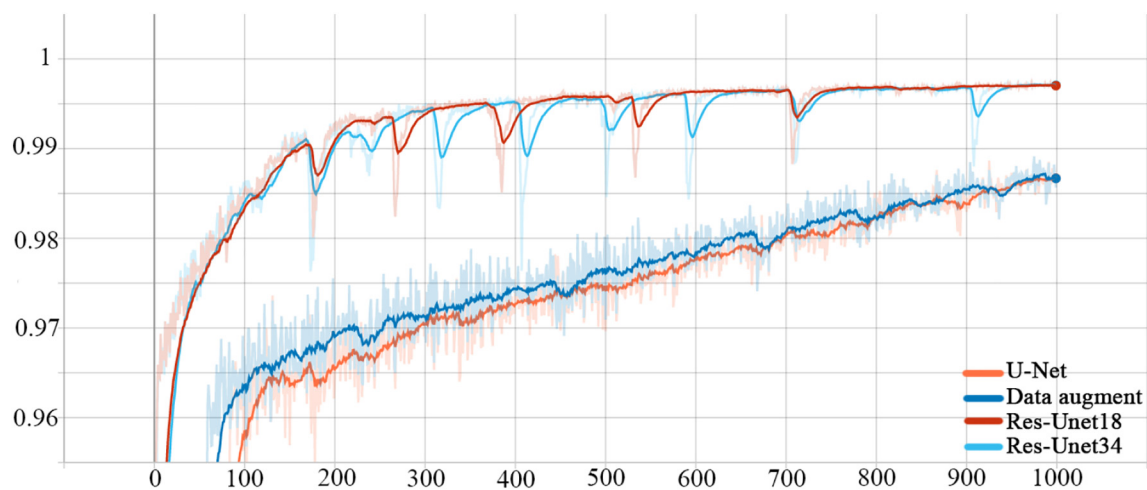


Fig. 6. The accuracy rate of models.

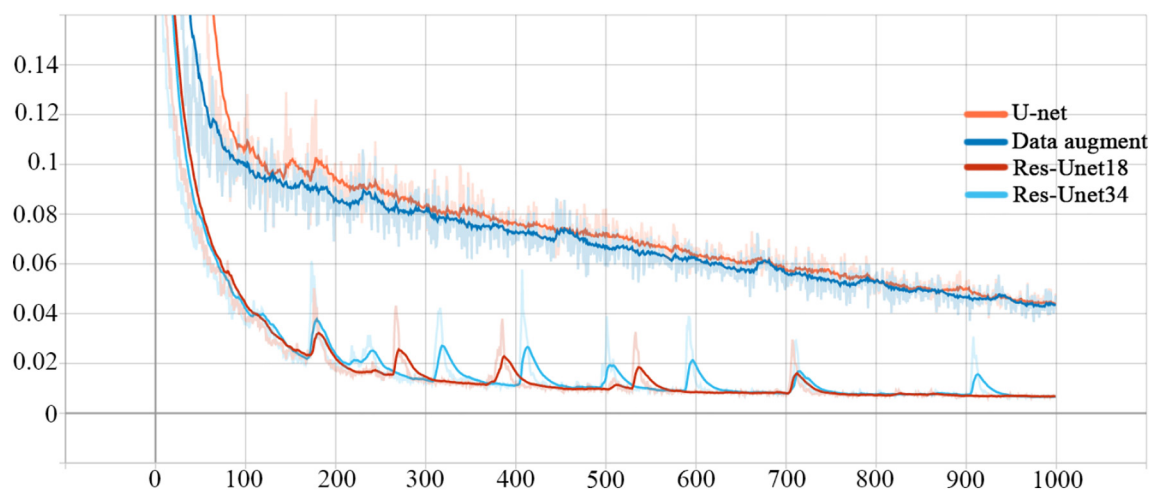


Fig. 7. The loss rate of models.

4.1. Quantitative evaluation

For the models of U-Net, Res-Unet18 and Res-Unet34, we carried out quantitative evaluation on 20 test images. Tables 1 and 2 show the

results of training the three models regarding accuracy and Dice scores. As shown in the tables, the average accuracy of Res-Unet18 was 5.48% higher than that of the original U-Net network, and the Dice score was also higher by 0.37%. Further, the Res-Unet18 has relatively low

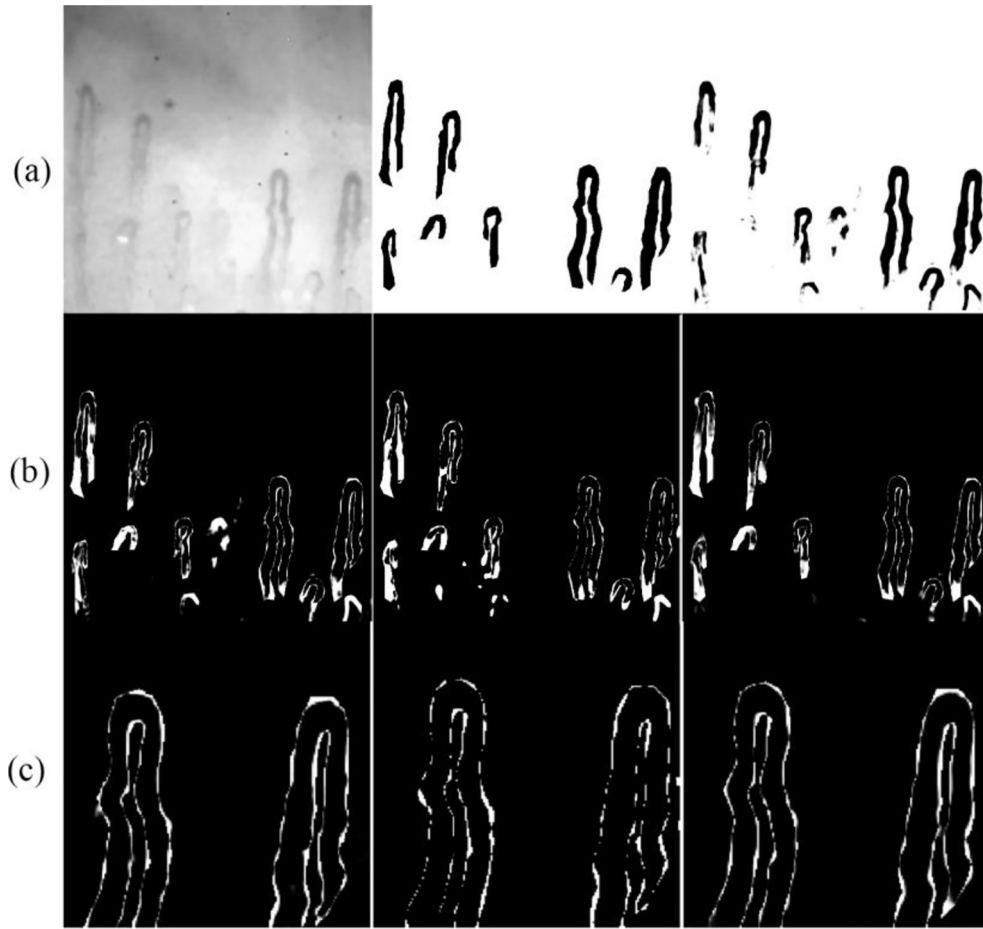


Fig. 8. Comparison of the segmentation results for normal capillaries. (a) input, label, and segmentation result of Res-UNet18. (b) differences between label and predictions of U-Net, Res-UNet18, and Res-UNet34 (different area is in white). (c) details of the differences.

standard deviations for accuracy and Dice scores, which indicates that the segmentation results from this proposed residual network model are relatively stable. Finally, the precision-recall curve and ROC curve of U-Net, Res-UNet18 and Res-UNet34 are shown in Fig. 5 where the best result performance is shown by Res-UNet18.

$$\text{Precision} = \frac{TP}{TP + FP} \quad (2)$$

$$\text{Recall} = \frac{TP}{TP + FN} \quad (3)$$

$$\text{TPR} = \frac{TP}{TP + FN} \quad (4)$$

$$\text{FPR} = \frac{FP}{FP + TN} \quad (5)$$

The training process curves of the networks are shown in Figs. 6 and 7. The abscissa represents the rounds per 100 iterations of the network, and the ordinate represents the accuracy or loss rate. The training accuracy of Res-UNet18 was the highest in the three models, and the loss rate decreased the fastest and had the lowest numerical value. The accuracy rate was 0.996, which was much higher than the original U-Net, and it converged smoothly after 560 rounds. This indicates that the residual network combined with U-Net can perform segmentation accurately.

We also examined the effect of adding data augmentation to the U-Net model. From the graphs, the training accuracy of the model that included data augmentation was higher than that of the original U-Net model, and the loss rate was also lower than that of the original model.

4.2. Quality evaluation

The input images had background noise and non-uniform lighting, and the resulting segmentation images showed no noise, as in Fig. 8(a). Fig. 8(b) shows that there is less white area for Res-UNet18 (center panel) than for the other models. As shown in Fig. 8(c), Res-UNet18 (center panel) has the least amount of white area on the edges, meaning that it has the highest coincidence with label image. As the Res-UNet18 was able to segment some capillary areas with low contrast, this model produced the best segmentation effect of the three models tested.

Compared with label images, amount of area that is different for the segment produced by Res-UNet18 is smaller than in the other models, as shown in Fig. 9(b). In Fig. 9(c), two crossed capillaries were enlarged for comparison; here in the regions where capillaries crossed, the segmentation produced by U-Net and Res-UNet34 had gaps, whereas Res-UNet18 segmented the whole crossed area.

The number of capillaries and the low quality had no effect on segmentation, and all capillaries were segmented in Fig. 10. The overall segmentation result from Res-UNet18 was better than that of the other models.

4.3. Result

The final nailfold capillary segmentation result was obtained by applying the mask operation to the original RGB images, as shown in Fig. 11, in which the hairpin-shaped area is segmented successfully from a low-quality image.

Compared to the original input images in Fig. 12(a), the results have standardized definite boundaries with a little error in Fig. 12(b). The

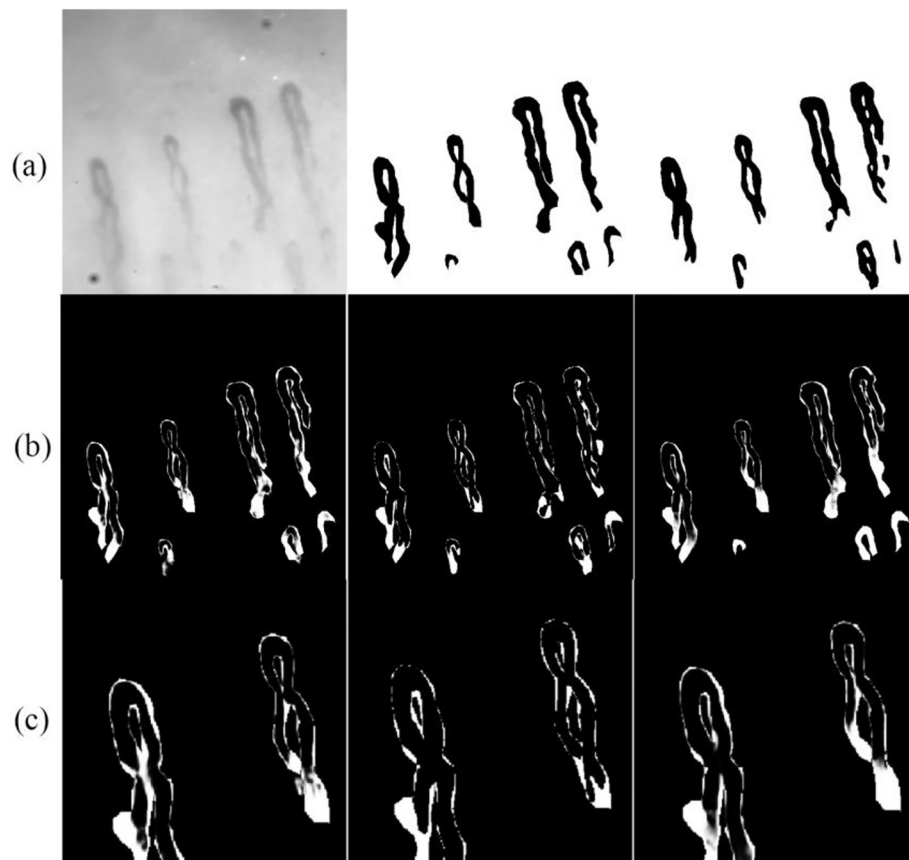


Fig. 9. Comparison of the segmentation results of crossed capillaries. (a) input, label, and segmentation result of Res-Net18. (b) differences between label and predictions of U-Net, Res-Net18, and Res-Net34 (different area is in white). (c) the details of differences.

diameter and density of the capillary can be measured and calculated more easily on the segmentation images than on the original images, and the segmentation images are free from background noise.

5. Conclusion

Microangiopathy corresponds to important clinical conditions (Ghizzoni et al., 2015), and such changes in the microvasculature can be detected in patients using nailfold capillaroscopy. In fact, studies have identified certain characteristics of nailfold capillaries that are associated with diseases; such characteristics include capillary dilatation (CD), capillary tortuosity (CT) and capillary enlargement (CE) (Pancar & Kaynar, 2018). Hence, being able to measure capillaries in the nailfold and assess their appearance is important for determining the clinical status of a disease.

To address the generally low quality of nailfold capillary images, this paper proposed a neural network combining U-Net and ResNet. This network's leaping connection, coding-decoding structure and deeper layers were able to preserve more details of the capillaries in poor-quality images.

Of course, some limitations in the research exist. The air bubbles in the immersion oil covered capillaries and spots reflected from the light source in the images could not be discriminated correctly; they were instead classified as capillary areas. Also, as the depth of the network increases, the network parameters also increase, affecting network performance. This aspect needs to be optimized in future experiments. Further, the equipment could be improved in future experiments, such as by using 420 nm (Bourquard et al., 2018) and 530 nm (Weekenstroo et al., 2015) light instead of white light for high contrast.

Nonetheless, of the three models tested, the Res-Net18 model had the best performance in experiments and evaluations. After the

segmentation image was produced, the morphology characteristics of the nailfold capillaries could be easily measured and calculated. Thus, even when only poor-quality images are available, this method can be used in clinical auxiliary judgement of related diseases.

Author's statement

I have made the substantial contribution to the design of the work and the data analysis; I have structured and revised the paper and I have approved to submit the manuscript; I agree to be accountable for all aspects of the work.

All persons who have made the substantial contributions to the work reported in the manuscript, including the persons helped the work in acknowledgement. I could signed the copyright with stand for all the authors for this manuscript.

Ethical approval

The study was conducted with the approval of the ethical committee of the Shanghai University.

Funding information

This work was funded by Natural Science Foundation of China (NSFC) (61575120, 61475095), and thanks for the support of the Key Laboratory of Specialty Fiber Optics and Optical Access Networks (SKLSFO2017-02 and SKLSFO2018-05).

Declaration of competing interest

The authors declare that they have no competing interests.

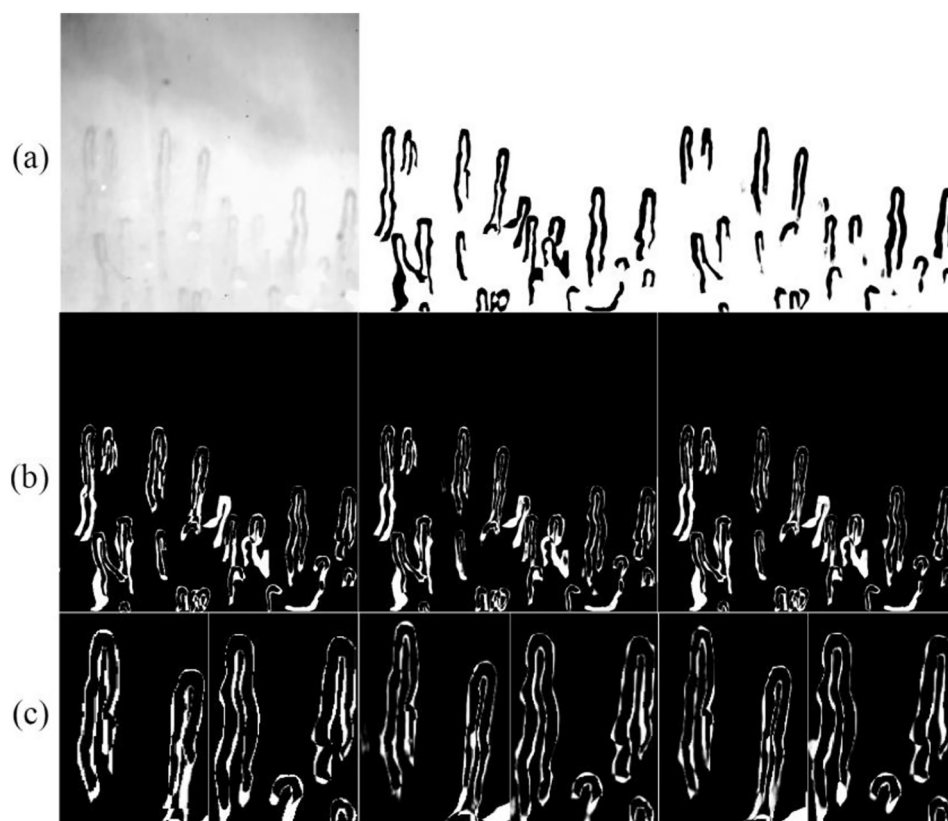


Fig. 10. Comparison of the segmentation results for more capillaries. (a) input, label, and segmentation result of Res-Net18. (b) difference between label and predictions of U-Net, Res-Net18, and Res-Net34 (different area is in white). (c) the detail of differences.

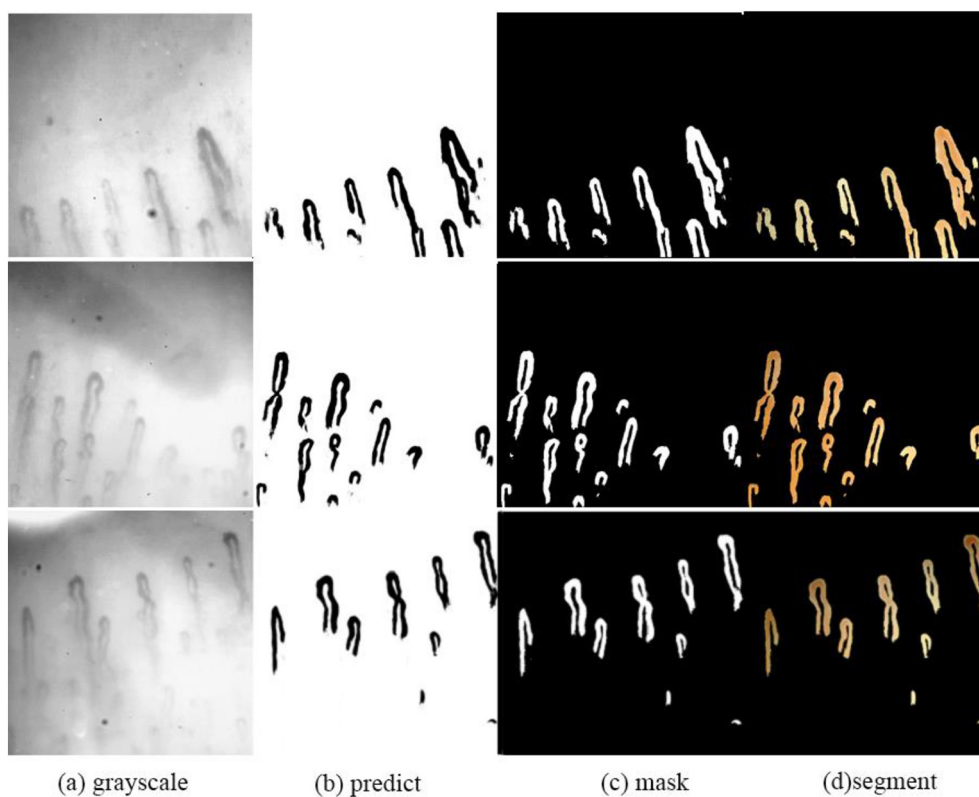


Fig. 11. Segmentations of Res-Net18. (a) the gray-scale input images. (b) the predictions of the Res-Net18 network. (c) mask: the inverse operation of binarization of predictions. (d) the segmentation after mask operation.

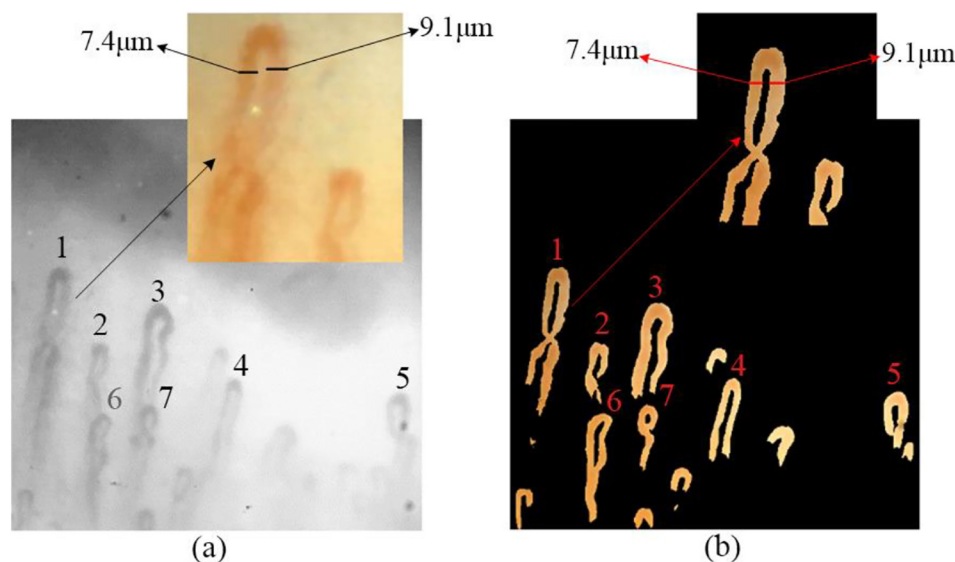


Fig. 12. Characteristics of the nailfold capillary. (a) the number of capillaries and diameter of the afferent loop and efferent loop from the original image. The boundary is blurry even for an RGB image. The diameter of the afferent loop and efferent loop are 7.4 μm and 9.1 μm . (b) the number of capillaries and diameter of the afferent loop and efferent loop from the segmented image. The boundary is clear after segmentation.

Acknowledgements

Thanks Professor Yu Wang from Shanghai University of Traditional Chinese Medicine for the help of the suggestions of nailfold capillaroscopy analysis.

References

- Al-Gindya, A., Al-Ahmadb, H., Qahwajic, R., Tawfika, A., 2008. A novel blind image watermarking technique for color rgb images in the dct domain using green channel. In: Mosharaka International Conference on Communications, Computers and Applications, pp. 26–31.
- Bengio, Y., Simard, P., Frasconi, P., 1994. Learning long-term dependencies with gradient descent is difficult. *IEEE Trans. Neural Netw.* 5 (2), 157–166.
- E. Bonacci, N. Santacroce, N. D'Amico, R. Mattace. "Nail-fold capillaroscopy in the study of microcirculation in elderly hypertensive patients," *Arch. Gerontol. Geriatr. Suppl.* 5, vol. 22, pp. 79–83, 1996, doi:[https://doi.org/10.1016/0167-4943\(96\)86918-4](https://doi.org/10.1016/0167-4943(96)86918-4).
- Bourquard, A., Pablo-Trinidad, A., Butterworth, I., et al., 2018. Non-invasive detection of severe neutropenia in chemotherapy patients by optical imaging of nailfold microcirculation. *Sci. Rep.* 8 (5301).
- Cutolo, M., Smith, V., 2013. State of the art on nailfold capillaroscopy: a reliable diagnostic tool and putative biomarker in rheumatology? *Rheumatology* 52 (11), 1933–1940.
- Cutolo, M., Melsens, K., Herrick, A.L., Foeldvari, I., Deschepper, E., De Keyser, F., Distler, O., Ingegnoli, F., Mostmans, Y., Müller-Ladner, U., 2018. Reliability of simple capillaroscopic definitions in describing capillary morphology in rheumatic diseases. *Rheumatology* 57 (4), 757–759. <https://doi.org/10.1093/rheumatology/kex460>.
- Doshi, N.P., Schaefer, G., Zhu, S.Y., 2015. An evaluation of image enhancement techniques for nailfold capillary skeletonisation. *Procedia Comput. Sci.* 60, 1613–1621.
- Etehad Tavakol, M., Fatemi, A., Karbalaie, A., Emrani, Z., Erlandsson, B.-E., 2015. Nailfold capillaroscopy in rheumatic diseases: which parameters should be evaluated? *Biomed. Res. Int.* 1–17. <https://doi.org/10.1155/2015/974530>.
- Faggioli, P., Tamburello, A., Sciascera, A., Gilardi, A.G., Mazzone, A., 2015. Nailfold video capillaroscopy in internal medicine. *Italian J. Med.* 9 (3), 234–242.
- Ghizzoni, Cecilia, Sebastiani, Marco, Manfredi, Andreina, Campomori, Federica, Colaci, Michele, Giuggioli, Dilia, Ferri, Clodoveo, 2015. Prevalence and evolution of scleroderma pattern at nailfold videocapillaroscopy in systemic sclerosis patients: clinical and prognostic implications. *Microvasc. Res.* 99, 92–95.
- Glorot, X., Bengio, Y., 2010. Understanding the difficulty of training deep feedforward neural networks. *J. Mach. Learn. Res.* 9, 249–256.
- Haoliang, Li, Lin, Zhe, Shen, Xiaohui, et al., 2015. A convolutional neural network cascade for face detection. In: *IEEE Conference on Computer Vision and Pattern Recognition*, pp. 5325–5334.
- He, K., Zhang, X., Ren, S., Sun, J., 2016. Deep residual learning for image recognition. In: *2016 IEEE Conference on Computer Vision and Pattern Recognition (CVPR)*, pp. 770–778.
- He, K., Zhang, X., Ren, S., Sun, J., 2016b. Identity mappings in deep residual networks. In: *Computer Vision and Pattern Recognition*. <https://arxiv.org/abs/1603.05027>.
- Ioffe, S., Szegedy, C., 2015. Batch normalization: accelerating deep network training by reducing internal covariate shift. In: *Machine Learning*. <https://arxiv.org/abs/1502.03167>.
- Karbalaie, Abdolamir, 2018. Novel analysis toolkit for capillaroscopic images. In: *Development and Clinical Evaluation*.
- Karbalaie, Abdolamir, Emrani, Zahra, Fatemi, Alimohammad, Etehadtavakol, Mahnaz, Erlandsson, Björn-Erik, 2019. Practical issues in assessing nailfold capillaroscopic images: a summary. *Clin. Rheumatol.* 38 (9), 2343–2354.
- Khan, Asifullah, Sohai, Anabia, Zahoor, Umme, Qureshi, Aqsa Saeed, 2019. A survey of the recent architectures of deep convolutional neural networks. In: *Computer Vision and Pattern Recognition*. <https://arxiv.org/abs/1901.06032>.
- Koscielny, J., Latza, R., Wolf, S., Kiesewetter, H., Jung, F., 1998. Early rheological and microcirculatory changes in children with type I diabetes mellitus. *Clin. Hemorheol. Microcirc.* 19 (2), 139–150.
- Lawrence Carin, PhD, Pencina, Michael J., PhD, 2018. On deep learning for medical image analysis. *J. Am. Med. Assoc.* 320 (11), 1192–1193.
- Li, Jia, 2011. Semantic Image Understanding: From the Web, in Large Scale and With Real-World Data. the department of computer science and the committee graduate studies of Stanford University.
- Li, L., Si, Y., Ma, B., et al., 2017. A novel medical image segmentation method based on GCBAC model. In: *10th International Symposium on Computational Intelligence and Design*, pp. 161–164.
- Mannarino, E., Pasqualini, L., Fedeli, F., Scricciolo, V., Innocente, S., 1994. Nailfold capillaroscopy in the screening and diagnosis of raynaud's phenomenon. *Angiology* 45 (1), 37–42.
- Nivedha, R., Brinda, M., Suma, K.V., Rao, B., 2016. Classification of nailfold capillary images in patients with hypertension using non-linear SVM. In: *2016 International Conference on Circuits, Controls, Communications and Computing*, pp. 1–5.
- Pancar, G.S., Kaynar, T., 2020. Nailfold capillaroscopic changes in patients with chronic viral hepatitis. *Microvasc. Res.* 129. <https://doi.org/10.1016/j.mvr.2019.103970>.
- Ronneberger, O., Fischer, P., Brox, T., 2015. U-net: convolutional networks for biomedical image segmentation. In: *International Conference on Medical Image Computing and Computer-Assisted Intervention*. Springer, pp. 234–241.
- Shelhamer, E., Long, J., Darrell, T., 2017. Fully convolutional networks for semantic segmentation. In: *IEEE Transaction on Pattern Analysis and Machine Intelligence*. vol. 39, no. 4, pp. 640–651.
- Shen, Dinggang, Wu, Guorong, Suk, Heung-Il, 2017. Deep learning in medical image analysis. *Annu. Rev. Biomed. Eng.* 19, 221–248. <https://doi.org/10.1146/annurev-bioeng-071516-044442>.
- Shigeharu, O., Hitoshi, Y., Atsuko, S., 2016. Medical image processing apparatus and method for processing medical image. *Med. Imag. Technol.* 14 (3), 207–211.
- Simonyan, K., Zisserman, A., 2014. Very deep convolutional networks for large-scale image recognition. In: *Computer Vision and Pattern Recognition*. <https://arxiv.org/abs/1409.1556>.
- Smith, V., Beecman, S., Herrick, A.L., Decuman, S., Deschepper, E., De Keyser, F., Distler, O., Foeldvari, I., Ingegnoli, F., Müller-Ladner, U., 2016. An EULAR study pilot study on reliability of simple capillaroscopic definitions to describe capillary morphology in rheumatic diseases. *Rheumatology* 55 (5), 883–890. <https://doi.org/10.1093/rheumatology/kev441>.
- Soomro, T.A., Afifi, A.J., Gaoetal, J., 2017. Boosting sensitivity of a retinal vessel segmentation algorithm with convolutional neural network. *Proc. IEEE Int. Confer. Digital Image Comput.* 1–8.
- Szegedy, C., Liu, W., Jia, Y., Sermanet, P., Reed, S., Anguelov, D., Erhan, D., Vanhoucke, V., Rabinovich, A., 2015. Going deeper with convolutions. In: *2015 IEEE Conference on Computer Vision and Pattern Recognition (CVPR)*, pp. 1–9.
- Szegedy, C., Ioffe, S., Vanhoucke, V., 2016. Inception-v4, Inception-ResNet and the Impact of Residual Connections on Learning. *arXiv Prepr. arXiv1602.07261v2*. vol. 131, no. 2, pp. 262–263.
- Tama, A., Mengko, T.R., Zakaria, H., 2015. Nailfold capillaroscopy image processing for morphological parameters measurement. In: *Instrumentation, Communications, Information Technology, and Biomedical Engineering (ICICI-BME), 4th International Conference on, IEEE*, pp. 175–179.
- Tian, Niu, Li, Xianghong, 1992. Clinical microcirculation examination manual. *Chin. J. Microcircul.* 2 (4), 48.
- Weekenstrop, Harm H.A., Cornelissen, Bart M.W., Bernelot Moens, Hein J., 2015. Green light may improve diagnostic accuracy of nailfold capillaroscopy with a simple digital video-microscope. *Rheumatol. Int.* 35, 1069–1071.
- Zhang, Kun, Zhang, Hongbin, Zhou, Huiyu, Crookes, Danny, Li, Ling, Shao, Yeqin, Dong, Liu, 2019. Zebrafish embryo vessel segmentation using a novel dual ResUNet model. *Comput. Intel. Neurosc.* 1–14. <https://doi.org/10.1155/2019/8214975>.